ADVANCED MATERIALS INTERFACES
www.advmatinterfaces.de

Nanostructured, Alkaline Titanate-Converted, and Heat-Treated Ti6Al4V Microspheres via Wet-Chemical Alkaline Modification and their ORR Electrocatalytic Response

Matthew D. Wadge, Matthew A. Bird, Andrzej Sankowski, Hannah Constantin, Michael W. Fay, Timothy P. Cooper, James N. O'Shea, Andrei N. Khlobystov, Darren A. Walsh, Lee R. Johnson, Reda M. Felfel, Ifty Ahmed, and David M. Grant**

This study describes the chemical conversion and heat treatment of Ti6Al4V microspheres (Ti6_MS), and the resulting effects on their electrocatalytic properties. The wet-chemical conversion (5.0 M NaOH, 60 °C, 24 h; Sample label: Ti6_TC) converts the top surface of the Ti6_MS powder into an ≈820 nm thick sodium titanate surface. Heat-treatment (Ti6_TC_HT) at 450 °C increases the stability of the surface, through partial titanate crystallization, while mitigating excess rutile formation. All samples are analyzed chemically (XPS, EDX, Raman, EELS), structurally (XRD and TEM), and morphologically (SEM, TEM), demonstrating the characteristic formation of sodium titanate dendritic structures, with minimal chemical, structural, and morphological differences due to the 450 °C heat-treatment. The effect of the preparation methodology on oxygen reduction reaction (ORR) electrocatalytic performance is also tested. The introduction of the sodium titanate layer changes the mechanism of the ORR, from a mixed 4 electron/2 electron pathway to a predominantly 2-electron pathway. By maintaining the microspherical nature of the material while also tuning the surface of the material toward different reaction mechanisms, a design strategy for new electrocatalyst materials is explored.

1. Introduction

Significant concern has been raised regarding depletion of non-renewable energy sources and the environmental effect of current energy consuming technologies as a result of worldwide technological development.[1] The movement toward greener and sustainable alternatives requires new technologies and alternative materials to achieve the ambitious goal of net zero carbon technologies by 2050.[2] Titanium dioxide (TiO_2) is a widely investigated material and considered as a ubiquitous low cost material to address the above concerns, such as its use in the transformation of solar energy into electricity, the production of hydrogen for energy storage, battery devices and chemical synthesis.[3,4] Despite its high band gap (E_{bg} = 3.2 eV[5]), and other favorable electronic properties such as stability in

M. D. Wadge, H. Constantin, R. M. Felfel, I. Ahmed, D. M. Grant
Advanced Materials Research Group
Faculty of Engineering
University of Nottingham
Nottingham NG7 2RD, UK
E-mail: matthew.wadge3@nottingham.ac.uk;
david.grant@nottingham.ac.uk

M. A. Bird, A. Sankowski, D. A. Walsh, L. R. Johnson
Nottingham Applied Materials and Interfaces Group
GSK Carbon Neutral Laboratory for Sustainable Chemistry
University of Nottingham
Jubilee Campus, Nottingham NG7 2TU, UK

M. W. Fay, A. N. Khlobystov
Nanoscale and Microscale Research Centre (nmRC)
University of Nottingham
Nottingham NG7 2RD, UK

T. P. Cooper
Advanced Component Engineering Laboratory
Faculty of Engineering
University of Nottingham
Nottingham NG8 1BB, UK

J. N. O'Shea
School of Physics and Astronomy
University of Nottingham
University Park, Nottingham NG7 2RD, UK

A. N. Khlobystov
School of Chemistry
University of Nottingham
University Park, Nottingham NG7 2RD, UK

R. M. Felfel
Physics Department
Faculty of Science
Mansoura University
Mansoura 35516, Egypt

R. M. Felfel
Advanced Composites Group
University of Strathclyde
Glasgow, Scotland G1 1XJ, UK

The ORCID identification number(s) for the author(s) of this article can be found under https://doi.org/10.1002/admi.202201523.

DOI: 10.1002/admi.202201523

electrochemical environments,[6,7] significant enhancement of these properties are needed to address the diverse challenges posed. Alkaline titanate structures have been of particular interest in a number of sectors, such as biomaterials[8–10] and energy storage,[11,12] due to their capability of apatite formation in vitro and in vivo, as well as large ion-exchange capacity, fast ion diffusion and intercalation, and high surface charge density, as described by Zhang et al.[13] These properties are a direct result of the crystal structure of titanate materials, whereby exchangeable cations sit in the interlayer between negatively charged 2D Ti-containing sheets.[14]

An advantage of wet-chemically converted titanates, as compared to those prepared through sintering, is the ability to generate unique nanoporous structures into the film structure.[8,9,15] Recent work highlighted the ability to generate such nanoporous titanate structures onto Ti6Al4V microspheres, broadening their applicability.[16] While studies have assessed the usage of hydrogen titanate nanotubes [17,18] for improved electron conductivity to aid catalytic performance of Pt-based catalysts, nanoporous titanate films without the formation of nanotubular structures, have not been fully investigated in this regard.

Here improved electrocatalytic functionality is postulated combining the ability to generate porous structures, which increases the potential reactive surface area, similar to those highlighted by Nikhil et al.,[19] with the potential electrocatalytic properties of titanates. To assess the potential of these wet-chemically modified surfaces in this study Ti6Al4V microspheres were converted via wet-chemical alkaline treatment to generate nanoporous sodium titanate surfaces. Furthermore, the effect of material stability through heat treatment of the modified microspheres was investigated in terms of electrocatalytic performance relative to the pre- and post-converted microspheres.

2. Experimental Section

2.1. Materials

2.1.1. Powders

Three different powders (untreated, titanate converted, and titanate converted plus subsequent heat treatment) with varying composition or modifications were prepared. The untreated Ti6Al4V powder (Timet Ti 6-4 PREP Powder; [–140 + 270] MESH; equivalent 53–105 μm) was used as the basis for subsequent modification in this study, and herein are labeled Ti6_MS.

2.1.2. Sodium Titanate Wet-Chemical Conversion

The Ti6_MS powders were suspended in an ≈5 M NaOH solution. The solution was prepared using NaOH pellets (99.9% purity; Sigma-Aldrich) by dissolving ≈19.99 g per 100 mL of distilled water. Falcon 15 mL (17 mm diam.; 120 mm length) Conical Sterile Polypropylene Graduated Centrifuge Tubes were used to store the suspensions. These were then sealed and heated in a low temperature Lenton furnace at 60 ± 2 °C for 24 h. Upon removal, the converted spheres were washed via filtration in deionized water to remove excess NaOH, before furnace drying at 100 °C for 1 h (in air), followed by storage within a desiccator until testing. The converted powders are herein labeled Ti6_TC.

2.1.3. Heat-Treatment

Portions of the converted powders were then heat-treated using a Lenton furnace in air with a ramp rate of 5 °C min^{-1} from room temperature to 100 °C then leaving them to dwell for 1 h. After the elapsed time, the furnace temperature was raised to 450 °C at the same ramp rate and dwell time, followed by furnace cooling to room temperature. A temperature of 450 °C was nominally chosen as it would ideally initiate crystallization of the formed titanate dendrites, without inducing excessive rutile formation (rutile formation occurs ≈600 °C[20]). The heat-treated powders are herein labeled as Ti6_TC_HT.

2.2. Characterization

2.2.1. Scanning Electron Microscopy (SEM) and Energy Dispersive X-Ray Spectroscopy (EDX)

Image acquisitions for higher resolution micrographs were conducted on a Field-Emission Gun Scanning Electron Microscope (JEOL 7100 FEG-SEM). Surface compositional analysis was determined via an Energy-Dispersive X-ray spectrometer (EDX) (Oxford Instruments) at a working distance of 10 mm, a beam voltage of 15 kV, while maintaining a minimum X-ray count of 250 000 counts.

2.2.2. Transmission Electron Microscopy (TEM)

Imaging was performed using a JEOL 2100+ transmission electron microscope (TEM) operating at an accelerating voltage 200 kV. The TEM samples were prepared by pressing TEM grids coated with a lacey carbon film (Agar Scientific, UK) into the titanate-converted, and heat-treated powders. Image analysis was conducted using a Gatan Ultrascan 1000XP CCD camera and Gatan Digital Micrograph software.

2.2.3. X-Ray Photoelectron Spectroscopy (XPS)

All samples were mounted onto stainless steel stubs using carbon sticky tabs. X-ray Photoelectron Spectroscopy (XPS) was conducted using a VG ESCALab Mark II X-ray photoelectron spectrometer with a monochromatic Al Kα X-ray source incident to the sample surface at ≈30°. Survey and high-resolution scans were conducted in addition to the measurement of adventitious C 1s for calibration: charge corrected to 284.8 eV. Parameters for acquisition were as follows: step size of 1.0 eV; number of scans set at 2; dwell time 0.2 s for survey scans, and a step size of 0.2 eV; number of scans set at 5; and dwell time of 0.4 s for high-resolution scans. Binding energies were

measured over a range of 0–1200 eV. All spectra were analyzed in CasaXPS constraining the Full Width at Half Maximum (FWHM) to the same value for all peak fit components for the same element. A Shirley background was employed for all peak fits, with appropriate line-shapes (either Gaussian–Lorentzian (GL), or Lorentzian Asymmetric (LA)) being used in accordance with XPS references.[21]

2.2.4. X-Ray Diffraction (XRD)

Sample crystallinity of all powders were analyzed using a Bruker D8 ADVANCE with DaVinci diffractometer (Cu Kα source, λ = 1.5406 Å, 40 kV, 40 mA) with a LYNXEYE 1D detector, in Bragg–Brentano mode. Powders were mounted into Perspex (polymethyl methacrylate; PMMA; Bruker) holders, ensuring the powder sits flush. Measurements were taken over a 2θ range from 30° to 100°; with a step size of 0.02° (2θ); and a step time of 0.2 s.

Calculation of crystallite size (τ) was conducted using the Scherrer equation[22]:

$$\tau = \frac{K\lambda}{\beta \cos\theta} \quad (1)$$

where K is a dimensionless shape factor, with a value close to unity (usually 0.9); λ is the X-ray wavelength; β is the line broadening at half the maximum intensity (FWHM), after subtracting the instrumental line broadening, in radians; and θ is the Bragg angle. Sizes were calculated using DIFFRAC.EVA software, with the five highest intensity peaks being used to determine the average crystallite size.

2.2.5. Raman Spectroscopy

Raman spectroscopy was conducted using a HORIBA Jobin Yvon LabRAM HR spectrometer. Microspheres, prior to analysis, were dispensed onto a Si (100) wafer. Spectra were acquired using a Quantum Ignis 660 nm Laser (100 mW power), 100× objective, and a 300 µm confocal pinhole. A 600 lines mm^{-1} rotatable diffraction grating along a path length of 800 mm was used for simultaneous scanning of multiple Raman shifts. Spectra detection was achieved through the use of a SYNAPSE CCD detector (1024 pixels) thermoelectrically cooled to –60 °C. Instrument calibration using the Rayleigh line at 0 cm^{-1} and a standard Si (100) reference band at 520.7 cm^{-1} was employed prior to spectra acquisition. A constrained time window of 10 s was employed for each spectrum recording with 10 accumulations per sample.

2.2.6. Electrocatalysis

10 mg of the titanate powders were mixed with 5 mg of Vulcan carbon (VC) and dispersed in ethanol (1 mL) and a 5% solution of Nafion in aliphatic alcohols (100 µL, Sigma Aldrich). The solution was stirred for 30 min using a magnetic stir bar. Sonication was avoided so as not to disrupt the microstructure of the materials.

A 5 mm glassy carbon rotating disc electrode (RDE; Pine Research, Durham, NC) was polished with 1, 0.3, and 0.05 µm alumina (Buehler, Coventry, UK) to a mirror finish. 10 µL of the above ink was dropcast onto the rotating electrode ($\varnothing$ = 5 mm, 100–200 rpm) and left to dry for ≈1 h at room temperature at 500 rpm.

Electrochemical testing was carried out using a model CHI760C potentiostat (CH Instruments) coupled with a modulated speed rotator from Pine Research. The working electrode was the coated glassy carbon electrode described above. A graphite rod counter electrode was used to prevent metallic contamination from the CE[23] and kept separate from the main electrolyte with a fritted glass tube filled with 0.1 M KOH. A Hg/HgO (0.1 M KOH) reference electrode was used. The reference potential was checked either against a in house built RHE or a Gaskatel Hydroflex RHE. The electrolyte was 0.1 M KOH.

The electrochemically active surface area (ECSA) of the coated electrode was determined by measuring cyclic voltammograms (CVs) at difference scan rates with a 100 mV window in a region in which no faradaic processes occurred. The oxygen reduction reaction (ORR) activity was measured by cyclic voltammetry between 0.8 and –0.2 V at 5 mV s^{-1}. The rotation rate was varied between 400 and 2500 rpm. When using O_2-saturated electrolyte, 20 cycles at 500 mV s^{-1} were carried out in the ORR region until a reproducible CV was observed, to ensure that saturation of the electrolyte had occurred. Blank CVs were recorded in N_2-saturated electrolytes and were subtracted from those recorded in O_2-saturated electrolyte to ensure only oxygen-related electrochemistry was investigated.

3. Results and Discussion

3.1. Morphological Characterization

Formation of nanoporous alkaline titanate structures via wet-chemical synthesis routes is relatively well-characterized within the literature, with a number of papers detailing their formation mechanism,[24–31] influence of porosity on endpoint applications, such as in biomedical implants,[32–34] as well as their cationic modification through ion-exchange reactions.[10,35,36] This study focused on the novel combination of the effect of 3D object sphericity (i.e., use of microspherical substrates[16]) on the formation of titanate materials, subsequent heat treatment to improve stability, and the use of modified microspheres for electrocatalytic materials.

Clear differences between the unconverted (Ti6_MS), converted (Ti6_TC) and heat treated (Ti6_TC_HT) powders are illustrated in the micrographs presented (**Figure 1**). The unconverted powder demonstrated a relatively smooth morphology (Figure 1A,B), with no noticeable features on the surface, except for small (≈100 nm) particulates (Figure 1C). Following the alkaline titanate conversion, nanoporous (≈100 nm) dendritic structures were observed, (Figure 1D–F), characteristic of wet-chemically converted titanate structures.[15] Similar structures were present in the Ti6_TC_HT powder (Figure 1G–I), with minor differences specifically regarding "webbing" between the titanate struts (Figure 1I). The probable cause for such a change is either minor formation of rutile crystals, or the subtle

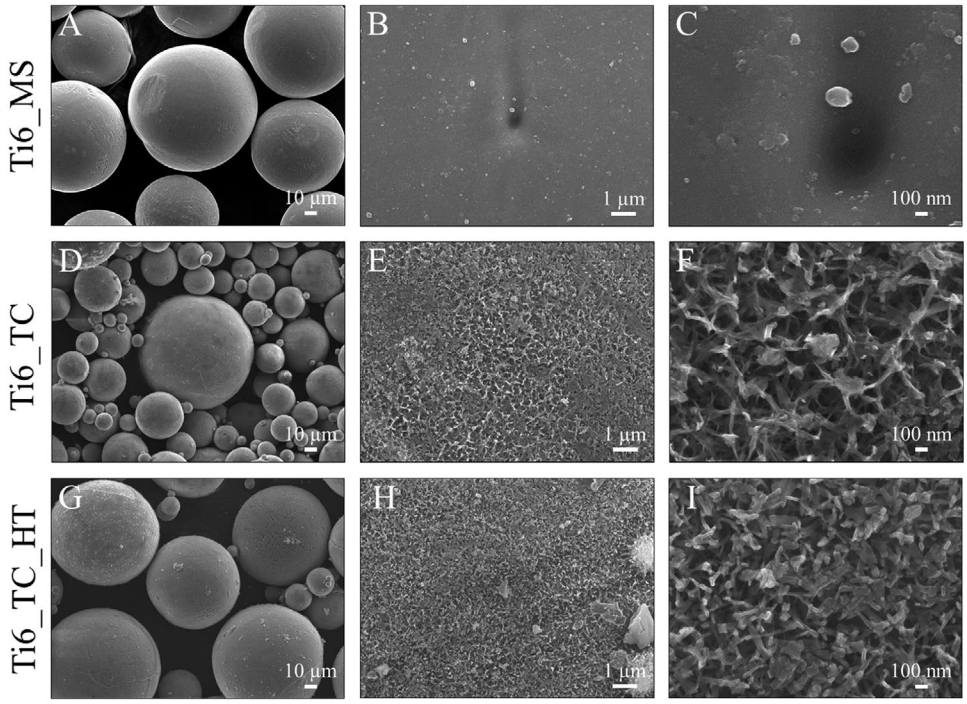

Figure 1. SEM micrographs of all samples tested. Samples shown: A–C) Ti6_MS, D–F) Ti6_TC, and G–I) Ti6_TC_HT.

modification/crystallization of the formed titanate surface. Sharpening of the XRD peaks following heat treatment is noted (Figure 4), which is likely due to increased crystallite size from ≈24 to 37 nm (derived from the Scherrer equation[37]). These changes are described in more detail in Section 3.2.

The thickness of the produced titanate coating was analyzed via ImageJ, with the average thickness found to be ≈822 ± 91 nm, which is consistent with studies by Wadge et al.,[16] Rastegari et al.,[38] Lee et al.,[39] and Yamaguchi et al.[40] for chemical conversion of Cp-Ti and Ti6Al4V structures, producing sodium titanate structures on the order of 0.5–1 µm. A representative micrograph is shown in **Figure 2**, detailing a region on the microsphere where delamination had occurred, with both the microsphere surface and the fractured through thickness of the titanate coating shown. No changes are noted between the pre- and post-heat-treated samples, and hence only a representative image of thickness is shown. The microspherical nature of the substrate, which possesses higher exposed surface areas, did not appear to modify the thickness of the produced structures, unlike the conversion of magnetron sputtered films with higher surface roughness which resulted in titanate thickness on the order of 1–1.5 µm.[15] The films presented in this study were comparable to other studies which converted bulk Ti discs (titanate thickness ≈1 µm[16]).

Further to SEM morphological analysis, TEM (**Figure 3**) was conducted to ascertain variations in surface morphology following titanate surface modification, as well as the subsequent heat-treatment. The Ti6_MS sample (Figure 3B) exhibited smooth, featureless surfaces, as expected. Following titanate conversion, as can be seen in Figure 3E, characteristic sodium titanate nanoporous structures were noted on the Ti6_TC microsphere surfaces, which are in agreement with other studies in the literature.[41–43] Following heat-treatment (Ti6_TC_HT), no clear morphological changes were noted, aside from the webbing mentioned previously (Figure 3H).

3.2. Crystalline, Structural, and Chemical Characterization

Verification of the effect of surface modifications on the microspheres was quantified through analytical techniques: XRD, EDX, XPS, and Raman spectroscopy. From the XRD data

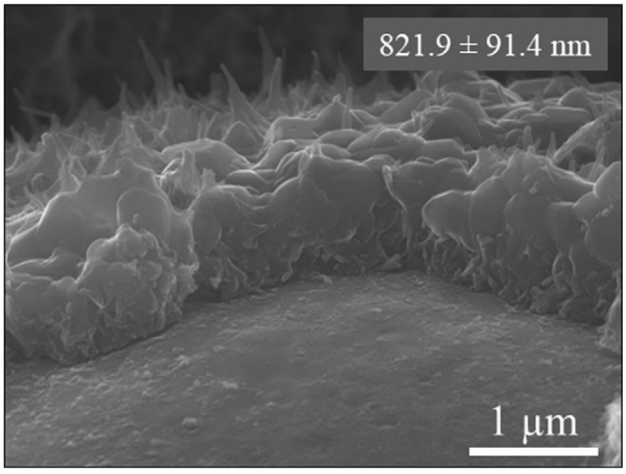

Figure 2. Representative SEM micrograph detailing the Ti6_TC surface, with and without the titanate structures due to fracturing. Multiple fractures on the surface were used to calculate the thickness of the titanate structure, included in the top right of the micrograph. Thickness value given as mean with standard error ($n = 15$).

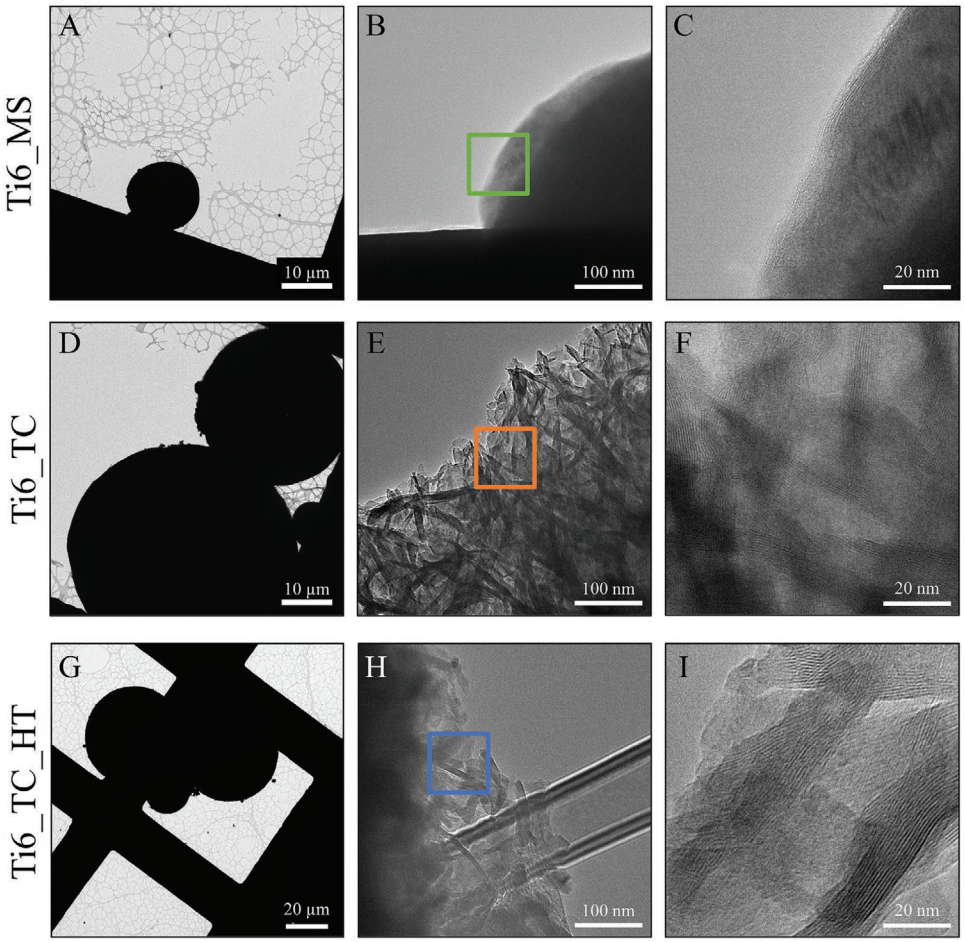

Figure 3. TEM micrographs of A–C) Ti6_MS, D–F) Ti6_TC, and G–I) Ti6_TC_HT showing the microspheres on the lacey carbon copper TEM grid and increasing in magnification to show the d-spacing of the surface structures. The three squares (green, orange, and blue) in (B), (E), and (H) highlight the higher magnified micrographs of individual struts in (C), (F), and (I), respectively.

(**Figure 4**), all powder samples (Ti6_MS, Ti6_TC, Ti6_TC_HT) demonstrated similar peak positions, with subtle changes in intensity as well as noticeable peak broadening in the unconverted and non-HT samples (Ti6_MS and Ti6_TC, respectively). Peak sharpening/narrowing with XRD analysis is usually consistent with growth of crystallite size, as stated previously, which is to be expected following heat treatment of the sample. All samples demonstrated multiple peaks, located at 35.5°, 38.6°, 40.5°, 53.4°, 63.6°, 71.1°, 74.9°, 77.0°, 78.2°, 82.8°, 87.7°, and 93.3° in 2θ, all corresponding to the HCP Ti PDF (ICDD 00-044-1294). Discrepancies between database and actual peak values were noted, with a "Tune Cell" correction being applied to best approximate actual diffraction data with database data. Unit cell parameters (a and c) were modified from 2.9505 and 4.6826, to 2.9210 and 4.6606 Å for a and c, respectively, pre- and post-heat treated.

An additional peak for the Ti6_TC and Ti6_TC_HT samples at ≈43.6°, but was not visible in the Ti6_MS sample, may correspond to titanate species (Figure 4 inset), or TiO_2(B) as reported by Rutar et al.,[44] and Marchand et al.,[45] however, the lack of additional peaks and the lower intensity means direct quantification was difficult. No further peaks were noted for the

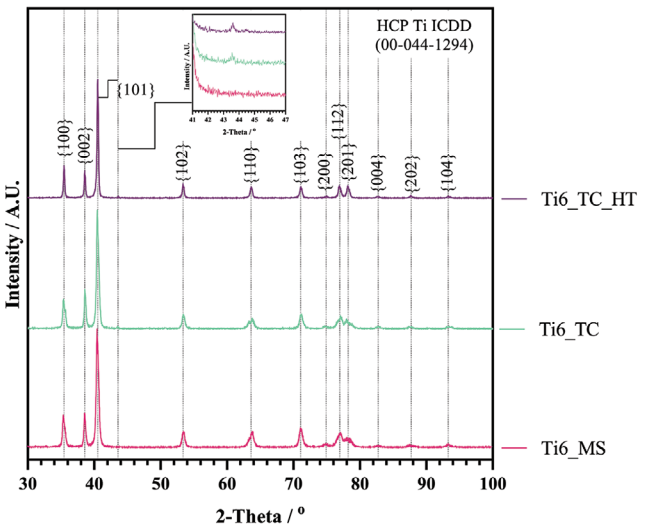

Figure 4. X-ray diffraction pattern of Ti6_MS, Ti6_TC, and Ti6_TC_HT powders. Inset graph details a small intensity peak located ≈43.6°, which may correspond to titanate species. The main peaks detailed correspond to HCP Ti (ICDD 00-044-1294).

samples post-titanate, or those with the additional post-heat-treatment, illustrating that no further phase change occurred. From the Scherrer calculations, the Ti6_MS and Ti6_TC samples exhibited similar crystallite sizes with 24.2 ± 3.0 and 23.6 ± 2.7 nm, respectively. However, following heat treatment this value increased to 37.3 ± 3.6 nm.

Formation of oxide species (TiO_2: brookite, anatase, or rutile) was not observed in either the titanate converted (Ti6_TC) or heat-treated samples (Ti6_TC_HT). This may be due to the penetration depth of the analysis utilized, or that the thickness of the oxide is insufficiently small to quantify (nm range).[46] In conjunction with XRD, diffraction analysis via TEM was also conducted to elucidate if any minor phase changes did occur. This analysis demonstrated similar diffraction patterns to those highlighted in Figure 4, with the only contribution being HCP Ti (PDF 00-044-1294), with smaller FWHM values noted for the Ti6_TC_HT samples, hence, these patterns have been highlighted in the supplementary information document (Figures S1 and S2, Supporting Information).

TEM analysis of Ti6_TC and Ti6_TC_HT also yielded d-spacing values which can be attributed to peaks present in the PXRD patterns, **Table 1**. The majority of d-spacing values could be attributed to peaks present in the PXRD patterns for both species, matching HCP Ti (00-044-1294), as seen previously. Similar to the previous XRD data, no additional species were noted.

Table 1. TEM d-spacing values and their corresponding PXRD peaks for both Ti6_TC and Ti6_TC_HT.

Sample ID	D-spacing [nm]	2θ [°]
Ti6_TC	0.47	38
	0.58	38
	0.67	40
	0.72	63
	0.91	–
	1.1	53
Ti6_TC_HT	0.26	35
	0.33	40
	0.39	53
	0.54	–
	0.72	–
	0.87	71

In order to determine any difference between Ti6_TC and Ti6_TC_HT with respect to element distribution and valence state of titanium, STEM EDX maps and EELS spectra were recorded. The EDX maps for Ti6_TC and Ti6_TC_HT, (**Figure 5**A,B, respectively) show the distribution of key elements present through the titanate microspheres. They both indicate a higher

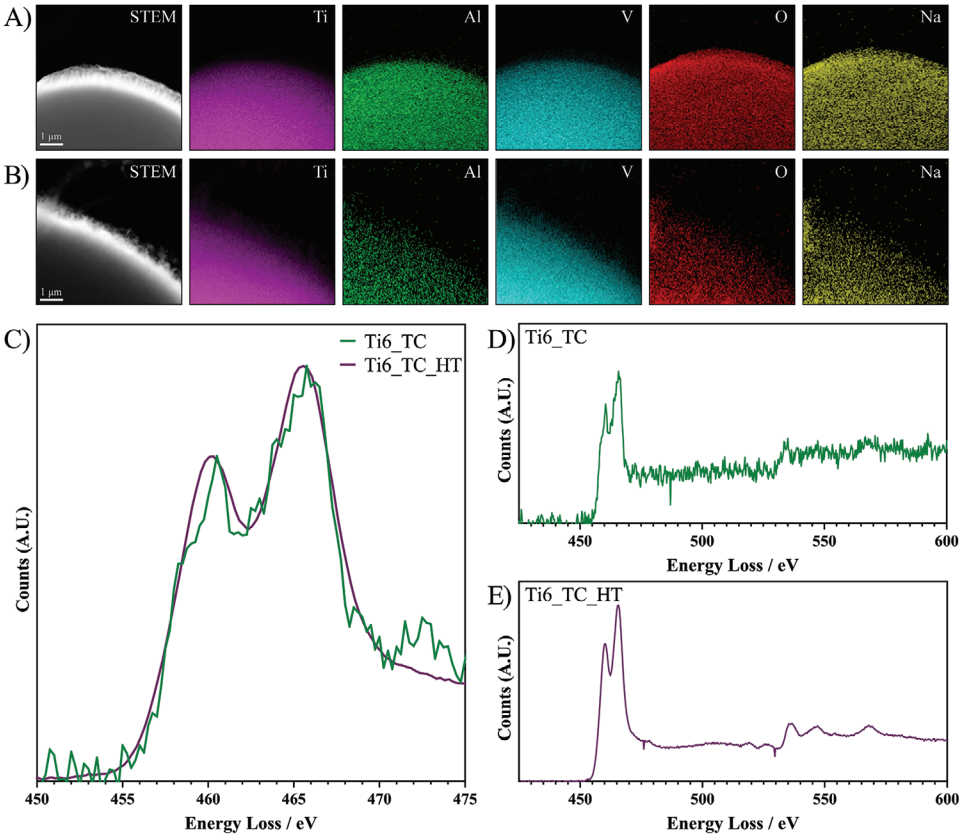

Figure 5. Combined STEM micrographs, EDX maps and EEL spectra for both the Ti6_TC and Ti6_TC_HT samples. A,B) STEM and EDX maps of Ti6_TC and Ti6_TC_HT, respectively; C) Compared EEL spectra for the Ti L 2,3 main edges; and D,E) EELS spectra showing Ti-L and O-K edges, from Ti6_TC and Ti6_TC_HT samples, respectively.

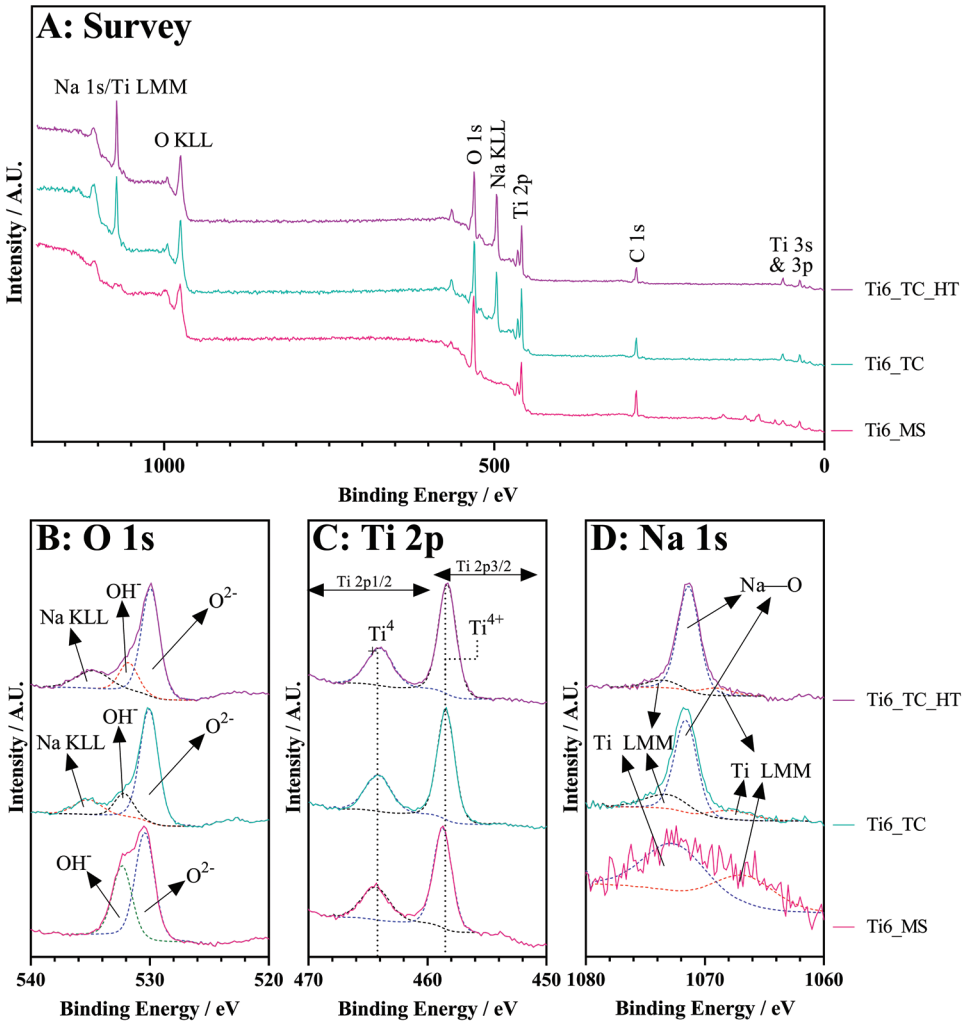

Figure 6. Survey and high-resolution spectra of Ti6_MS, Ti6_TC, and Ti6_TC_HT samples. A) Survey spectra; B) O 1s high-resolution spectra; C) Ti 2p high-resolution spectra; D) Na 1s high-resolution spectra.

density of titanium toward the core and a sparse amount near the edge, which was expected. The sodium map for Ti6_TC shows an increased density of sodium at the fringes of the spheres.

To see if any changes could be seen in the valence state of titanium through heat treatment, EELS spectra were recorded in the titanium $L_{2,3}$ edge region, from which it is possible to determine the valence state of titanium present. A comparison between the Ti6_TC and Ti6_TC_HT in this region (Figure 5C) shows that the valence state before and after heat treatment remains the same, with peak positions of 459 and 465 eV (Ti^{4+}) as described by Sankararaman et al.,[47] as there is no change in the peak shape for the key region which determines valence state. The wide scans for both these samples (Figure 5D,E) again show little variation between the two samples with both presenting a similar O k edge as well.

XPS analysis was conducted (**Figure 6** and **Table 2**) to understand the chemical surface variances due to the alkaline

Table 2. EDX and XPS elemental composition of the native Ti6Al4V, sodium titanate converted, and heat-treated powders. Values given are mean values ± Standard Error of the Mean (SEM; $n = 5$).

Sample ID	Elemental Composition [at%]									
	Na		Ti		O		Al		V	
	EDX	XPS	EDX	XPS	EDX	XPS	EDX	XPS	EDX	XPS
Ti6_MS	0	0	86.5 (± 0.2)	25.7 (± 1.2)	0	74.3 (± 1.2)	9.8 (± 0.3)	0	3.7 (± 0.1)	0
Ti6_TC	3.9 (± 0.3)	19.9 (± 0.6)	34.5 (± 1.3)	19.2 (± 0.4)	57.0 (± 1.3)	60.9 (± 0.7)	2.5 (± 0.4)	0	2.1 (± 0.6)	0
Ti6_TC_HT	5.4 (± 0.3)	20.8 (± 0.6)	31.3 (± 0.4)	15.6 (± 0.4)	59.1 (± 0.3)	63.6 (± 0.7)	2.9 (± 0.1)	0	1.4 (± 0.1)	0

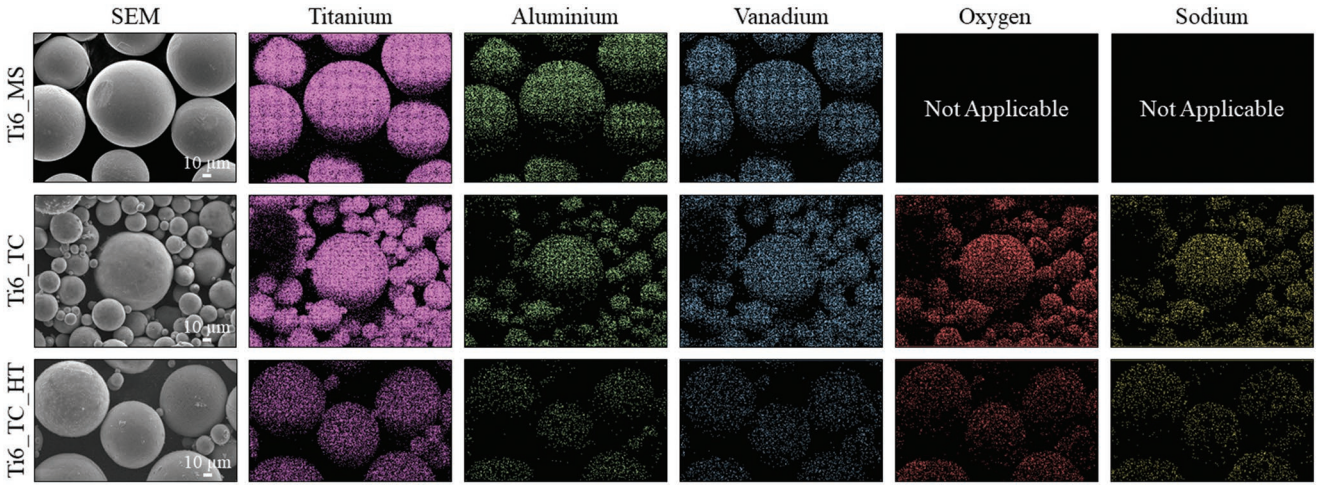

Figure 7. SEM micrograph and EDX mapping of Ti6_MS, Ti6_TC, and Ti6_TC_HT samples, illustrating the homogeneity and intensity of Ti, Al, V, O, and Na elements.

solution and heat treatments, in conjunction with EDX measurements (**Figure 7** and Table 2). Specific contributions and their binding energies were analyzed, with noticeable differences being noted for Na 1s, O 1s, and Ti 2p spectra for pre- and post-titanate converted samples, as well as heat treated counterparts. For the Ti6_MS samples, the O 1s peak was comprised of two components were noted in all Ti sample types, located at ≈530.2 (66.4%) and 532.3 (33.6%) eV, corresponding to O^{2-}, and OH^{-}/Surface O, respectively. For the Ti 2p doublet peaks, one deconvoluted state (458.5 eV 2p 3/2) was found corresponding to Ti^{4+}, indicative of TiO_2, correlating with EELs (Figure 5). No Na 1s peak was seen, however, two Ti LMM peaks were noted in a similar binding energy range, which was expected. These results match the expected surface conditions of Ti/Ti alloy materials, since the surface readily passivates in exposure to atmospheric oxygen, forming a relatively thin (≈1.5–25 nm) oxide layer.[48]

Following titanate conversion (Ti6_TC), modifications were noted in the number of peak contributions and binding energy positions. The O 1s peak detailed an increase in the number of peak components from two to three with the addition of the Na KLL Auger peak at ≈535.2 eV (13.9%), with the O^{2-} and OH^{-} shifting to 530.0 (71.5%) and 532.2 (14.6%) eV, respectively. The Ti 2p peak shifted slightly to 458.4 eV. An additional peak for the Ti6_TC sample was noted at 1071.6 eV (65.6%) corresponding to Na–O, characteristic of sodium titanate structures. Collectively, these results correlate well with previous studies by Takadama et al.,[49] Zárate et al.,[50] and the present authors,[15] which detail the formation of sodium hydrogen titanate species, such as $Na_2Ti_3O_7$; $Na_2Ti_3O_7 \cdot nH_2O$; $Na_2Ti_2O_5 \cdot nH_2O$, $Na_xH_{2-x}Ti_3O_7$, and/or mixtures of these phases.

After the heat treatment stage (Ti6_TC_HT), subsequent modifications were noted in the XPS analysis. The O 1s peak remained constant in number of components, but shifts were noted in peak positions. The new peak positions were 529.9 (64.2%), 531.8 (16.9%), and 534.8 (18.9%) eV, for O^{2-}, OH^{-}, and Na KLL, respectively. The Ti 2p peak shifted slightly to 458.3 eV and the Na 1s shifted to 1071.4 eV (82.7%). Similar to previous analyses, such as SEM (Figure 1) and XRD (Figure 4), no additional changes are noted both chemically and morphologically, aside from webbing formation between struts, following heat treatment. Ti can occupy 4 valence states, namely 0, 2+, 3+, and 4+. Typically, associated peak positions of the 2p3/2 peak for these states are ≈453.9, 455.3, 457.1, and 458.5 eV, however, some variance (±0.2–0.4 eV) can be seen from the literature.[9,51–53] Potentially, a shift to lower eV of the 4+ state may indicate a shift from anatase (≈458.6 eV) to rutile (≈458.5 eV), however, this may be within error due to the use of adventitious C as described by Biesinger et al.[51]

EDX measurements (Table 2 and Figure 7) detailed significant differences between the Ti6_MS, Ti6_TC, and Ti6_TC_HT samples. The native Ti6_MS powder, as expected, only contained Ti, Al and V at ≈86.5 (90.1), 9.8 (5.8), and 3.7 (4.1) at% (wt%), respectively. As detailed previously, due to the passivation of the microsphere surface, combined with the penetration depth of X-rays within XPS (5–10 nm[46]), only Ti and O were seen in XPS at levels of 25.7 and 74.3 at%, respectively. Following conversion, the Ti6_TC sample showed an increase in Na and O content to ≈3.9 and 57 at%, respectively, while Ti reduced to ≈34.5 at%. Compared to the XPS measurements, Na and O were shown to be concentrated, particularly the case for Na, in the surface and demonstrates a clear diffusion gradient as seen in the literature.[15,54,55] Further differences were noted following heat treatment (Ti6_TC_HT), with additional increases seen for Na and O to ≈5.4 and 59.1 at%, respectively, as a result of increased diffusion.[56] Similar trends were also seen in the XPS results. Ti exhibited a further decrease to ≈31.3 at%. All samples exhibited homogeneous distribution of all elements throughout the microspheres (Figure 7).

Raman spectral analysis (**Figure 8**) showed for the Ti6_MS powders, no distinct bands were noted, illustrating the Ti6_MS samples was mostly Raman inactive. Following NaOH treatment, peaks at ≈285, 440, and 900 cm^{-1}, with broad peaks around 630–850 cm^{-1} were seen, in the Ti6_TC sample and were consistent with sodium hydrogen titanate ($Na_xH_{2-x}Ti_3O_7$) and titanate species.[40] Following heat-treatment (Ti6_TC_HT), bands were located at ≈255, 440, 610, and 900 cm^{-1} corresponding to rutile species, despite not being seen in XRD or TEM analyses. This suggests that rutile nucleation has started

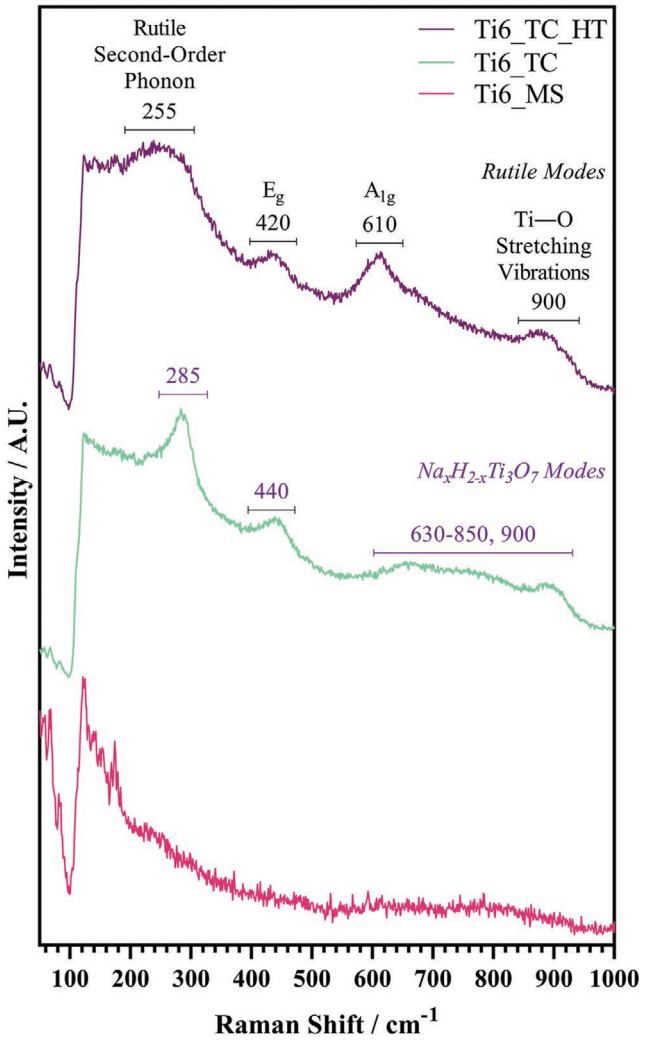

Figure 8. Raman spectra of Ti6_MS, Ti6_TC, and Ti6_TC_HT samples.

to occur and is in small enough quantity to only be seen by Raman analysis. Specifically, the bands at ≈255, 440, 610, and 900 cm^{-1} correlated with rutile second order phonons (Ti_2O_3), E_g, A_{1g}, and Ti–O stretching vibrations (TiO_4 tetrahedra) modes, respectively.[57] Broadening of the 255 and 900 cm^{-1} is likely due to overlapping of the titanate and TiO_2 bands. In the Ti6_TC sample, there is a small, very broad bump at ≈660 cm^{-1}, which when correlated with the peaks at ≈285 and 440 cm^{-1}, suggests Ti–O–Ti stretching in edge-shared TiO_6. Furthermore, the presence of the shifted peak at ≈900–905 cm^{-1} suggests stretching vibration of the short Ti—O bonds in distorted TiO_6 unit. The formed bands highlighted above match analysis by Viana et al.,[58] as well as other studies, following titanate conversion.[58–61] The differences noted between the Ti6_TC and Ti6_TC_HT samples are interesting, and despite the lower temperature used, some phase change has occurred due to both the titanate and heat-treatment stages, and suggested the later has induced nucleation of Rutile phases.[62] Furthermore, the micrographs presented in Figure 1 detail morphological modification to the microsphere surface, with clear formation of crystallites between the already formed titanate structures.

3.3. ORR Activity in Alkaline Electrolyte Environments

The ability of the materials to reduce oxygen in a basic environment, by first mixing them with conductive Vulcan carbon XC72R in a 4:1 ratio with a Nafion binder, was investigated. The ink was dropcast onto a GC rotating disc electrode to give a mass loading of ≈0.9 mg cm^{-2}. Unless otherwise specified, all current densities are normalized to the geometric area of the electrode. **Figure 9**A shows the rotating disc electrode voltammograms of each of the three materials in O_2-saturated 0.1 M KOH. All three materials showed very similar ORR onset potentials (defined as a current density of –0.1 mA cm^{-2}) of around 0.70 V.

When the specific current density is reported, the current is normalized to the electrochemically active surface area (ECSA) of the coating is used. The ECSA is determined from the double-layer capacitance of the material calculated from the gradient of the straight line derived from a plot of the scan rate versus non-Faradaic current. A representative example of this is given in Figure 9B for Ti6_TC. The slope is then divided by 22 μF cm^{-2} (the specific capacitance value associated with carbon-containing electrocatalysts).[63,64] The ECSA of the electrocatalysts mixed with Vulcan carbon are 8.1, 10.1, and 14.7 cm^2 for Ti6_MS, Ti6_TC, and Ti6_TC_HT, respectively.

Elucidation of the mechanism was achieved through Koutecký–Levich (K–L) analysis. For this, the rotation rate was varied between 400 and 2500 rpm and the inverse of the current reached at the specified potential (in this case 0.5 V vs RHE where the plateau begins) was plotted against the inverse of the rotation rate. This plot follows the relationship given the in the K–L equation (i is the measured current, i_K is the kinetic current, and i_L is the mass-transport limited current):

$$\frac{1}{i} = \frac{1}{i_K} + \frac{1}{i_L} \tag{2}$$

where

$$i_L = 0.620nFAD_O^{2/3}\nu^{-1/6}\omega^{1/2}C_O \tag{3}$$

n = number of electrons transferred, F = Faraday's constant, A = geometric area of the electrode, D_O = diffusion coefficient of oxygen (1.93×10^{-5} cm^2 s^{-1}), ν = kinematic viscosity (1.09×10^{-2} cm^2 s^{-1}), ω = rotation rate (rad s^{-1}), and C_O = concentration of oxygen (1.26×10^{-6} mol cm^{-3}). Values for the diffusion coefficient, kinematic viscosity, and saturation concentration of oxygen taken from.[65]

Figure 9C presents the results of this Koutecký–Levich analysis at 0.50 V versus RHE. The slopes obtained are the inverse of the mass-transport limited currents i_L which can be used to calculate the number of electrons transferred at that potential using the above-described equation. The value of n was calculated between 0.5 and 0.4 V, and given ± 2 standard deviations. Ti6_MS has n = 3.08 ± 0.17, whereas Ti6_TC and Ti6_TC_HT have n = 1.98 ± 0.10 and n = 1.83 ± 0.14, respectively. The first result indicates that Ti6_MS electrocatalyses the ORR through a mixture of the direct 4 electron pathway and the 2 × 2e electron pathway which proceeds via a peroxide intermediate, whereas the latter two materials are selective toward

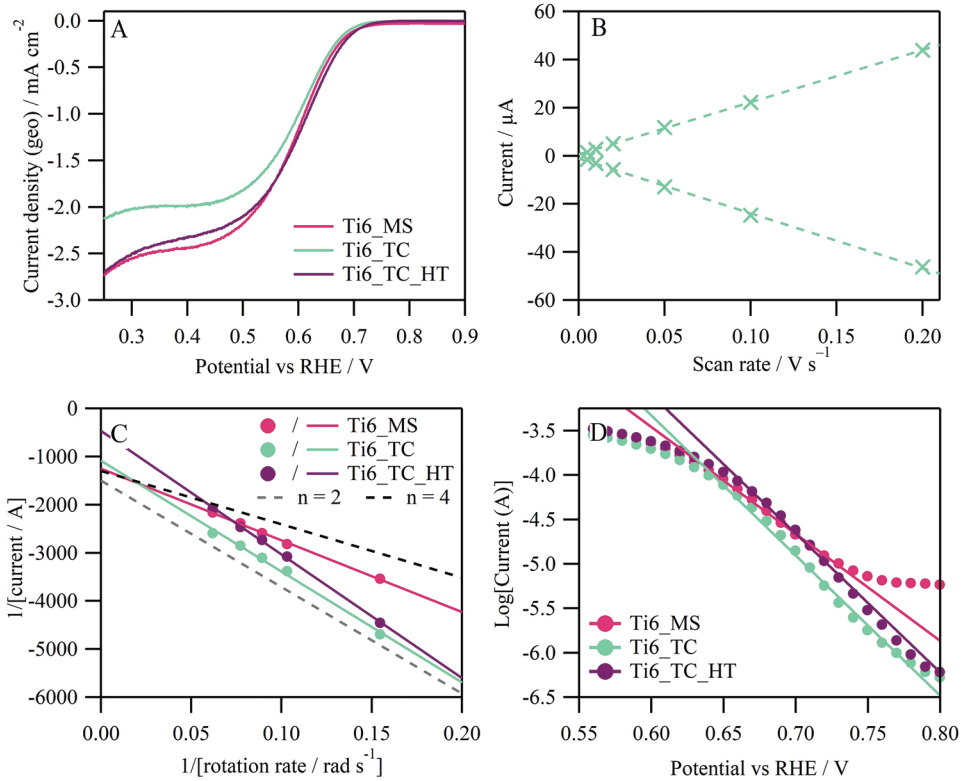

Figure 9. A) Rotating disc electrode voltammograms showing the oxygen reduction reaction in O_2-saturated 0.1 mol dm^{-3} KOH. Measured at 5 mV s^{-1} and 1600 rpm. N_2-purged LSVs were subtracted. Currents are normalized to the geometric area of the electrode disc (0.196 cm^2). B) Plot of the relationship between scan rate and the non-Faradaic current that passes at 0.85 V for Ti6_TC. C) Koutecký–Levich plot of the inverse rotation rate against the inverse current measured at 0.5 V versus RHE. The gray and black dotted lines show the theoretical slopes expected for $n = 2$ and $n = 4$ (with arbitrary intercepts). D) Potential versus log $|i|$ extracted from the LSVs in (A). Tafel slopes fitted to the linear region of these plots. The slopes for Ti6_MS, Ti6_TC, and Ti6_TC_HT are 82.8 ± 0.9, 62.7 ± 1.3, and 63.5 ± 1.2 mV dec^{-1}, respectively, where errors are given as ±2 s.d.

the 2 × 2e electrocatalysis pathway.[66–68] Further evidence for the unconverted material being mechanistically different to the converted materials is provided by the Tafel slopes presented in Figure 9D. Both Ti6_TC and Ti6_TC_HT have Tafel slopes close to 60 mV dec^{-1} (62.7 and 63.5 mV dec^{-1}), whereas Ti6_MS exhibits a Tafel slope 82.8 mV dec^{-1}. For the ORR, the archetypical Tafel slopes are 120, 60, and 40 mV dec^{-1} depending on the rate determining step.[68] The slope of 60 mV dec^{-1} is indicative of a pseudo 2 electron reaction as the rate determining step, which is possible with the 2 × 2 pathway.[66] That Ti6_TC's Tafel slope falls between two of these values further suggests a mixed mechanism is present.

The intercept of the Koutecký–Levich slope presented in Figure 9B is the inverse of the kinetic current. This is the current that would flow in the absence of any mass-transport limitations. A higher kinetic current is preferred as this is associated with faster kinetics. When reported normalized to the geometric surface area, Ti6_TC_HT had a kinetic current over twice that of the Ti6_TC and Ti6_MS. However, this is in part due to the high surface area of the material imparted during the heat treatment process. Ti6_TC_HT has a surface area (14.7 cm^2) 1.45 times greater than Ti6_TC (10.1 cm^2) as determined by the double-layer capacitance measured as described above. Ti6_MS had the lowest surface area of 8.1 cm^2.

Given the variation in surface areas of the materials, the geometrically normalized kinetic current does not give information on the intrinsic activity of the material. To this end, the currents were renormalized to the specific current densities. In this manner, Ti6_TC_HT still has the highest kinetic current of –0.14 mA cm^{-2}, whereas Ti6_MS and Ti6_TC have similar kinetic currents of –0.099 and –0.091 mA cm^{-2}.

Combined, this suggests that the heat-treatment both benefits the electrocatalytic activity by increasing the activity of the active sites and also by enhancing the morphology of the material through a higher surface area exposing more sites. Heat treatment is thus suggested as a potential strategy to enhance the kinetics of an electrocatalyst without changing the mechanism through which the reaction proceeds.

These results are summarized in **Table 3**.

4. Conclusions

This study presented the wet-chemical production of nanoporous sodium titanate films onto microspherical Ti-6Al-4V substrates, with and without subsequent 450 °C heat-treatment, and the effect the surface morphology and chemistry have on its ORR potential. Morphological (SEM, TEM) and chemical (XPS, EELS, EDX, and Raman) analyses demonstrated successful

Table 3. Comparison of the electrochemical properties of the three materials. Errors are given as ± 2 standard deviations.

Sample ID	ECSA [cm^2]	Geometric kinetic current density [mA cm^{-2}]	Specific kinetic current density (at 0.5 V) [mA cm^{-2}]	Number of electrons (average between 0.4 and 0.5 V)	Tafel slope [mV dec^{-1}]
Ti6_MS	8.1	−4.08	−0.099	3.08 ± 0.17	82.8 ± 0.9
Ti6_TC	10.1	−4.70	−0.091	1.98 ± 0.10	62.7 ± 1.3
Ti6_TC_HT	14.7	−10.87	−0.146	1.83 ± 0.14	63.5 ± 1.2

formation of sodium titanate layers onto the alloy microspheres. Clear differences were noted via Raman with the post heat-treatment demonstrating a transition from a sodium titanate dominant surface to contain Rutile modes. However, these changes were not easily seen in XRD, XPS and EDX. TEM was employed to try and differentiate any key differences between the pre- and post-heat-treated titanate substrates. No clear difference was seen between the two species and most d-spacings can be designated to PXRD peaks. Those which could not be designated are most likely due to other species on the surface, which are in too small a concentration to be detected by PXRD.

The addition of the sodium titanate layer on the microspheres changed the mechanism by which the oxygen reduction reaction proceeded. Without the layer, a mix of both the direct 4 electron reduction and the 2 × 2 electron reduction was observed, whereas when the layer was present, a preference for the 2 × 2 electron reduction pathway via a peroxide intermediate was observed. The heat-treatment did not change this specificity, further showing that it was the sodium titanate layer that caused the change. The heat-treatment did, however, slightly improve the kinetics of the 2 × 2 electron reduction pathway. The heat-treatment greatly increased the activity of the material when considered on a geometric basis as it substantially increased the surface area of the material. Thus, the addition of a sodium titanate or similar layer could be used in the design of future electrocatalysts while maintaining the morphology of the underlying material.

Supporting Information

Supporting Information is available from the Wiley Online Library or from the author.

Acknowledgements

This work was graciously funded through an Engineering and Physical Sciences Research Council (EPSRC) Doctoral Prize Fellowship (Grant code: EP/T517902/1), as well as support from an EPSRC equipment grant for SEM and TEM access (Grant code: EP/L022494/1). The authors would like to thank all technical help within the Wolfson building and nmRC facilities at the University of Nottingham. The authors thank the University of Nottingham's Propulsion Futures Beacon for funding toward this research.

Conflict of Interest

The authors declare no conflict of interest.

Data Availability Statement

The data that support the findings of this study are available from the corresponding author upon reasonable request.

Keywords

alkaline ORR, alkaline titanate, nanoporous surfaces, Ti6Al4V microspheres, wet-chemical conversion

Received: July 11, 2022
Revised: October 24, 2022
Published online: December 2, 2022

[1] M. F. Ashby, *Materials and Sustainable Development*, Butterworth-Heinemann, Cambridge, MA, USA **2015**.
[2] J. Deutch, *Joule* **2020**, *4*, 2237.
[3] Z.-Z. Jiang, Z.-B. Wang, Y.-Y. Chu, D.-M. Gu, G.-P. Yin, *Energy Environ. Sci.* **2011**, *4*, 728.
[4] Q. Lv, M. Yin, X. Zhao, C. Li, C. Liu, W. Xing, *J. Power Sources* **2012**, *218*, 93.
[5] N. Serpone, *J. Phys. Chem. B* **2006**, *110*, 24287.
[6] X. Lang, X. Chen, J. Zhao, *Chem. Soc. Rev.* **2014**, *43*, 473.
[7] S. Y. Huang, P. Ganesan, S. Park, B. N. Popov, *J. Am. Chem. Soc.* **2009**, *131*, 13898.
[8] M. D. Wadge, B. W. Stuart, K. G. Thomas, D. M. Grant, *Mater. Des.* **2018**, *155*, 264.
[9] M. D. Wadge, J. McGuire, B. V. T. Hanby, R. M. Felfel, I. Ahmed, D. M. Grant, *J. Magnesium Alloys* **2021**, *9*, 336.
[10] S. Yamaguchi, S. Nath, Y. Sugawara, K. Divakarla, T. Das, J. Manos, W. Chrzanowski, T. Matsushita, T. Kokubo, *Nanomaterials* **2017**, *7*, 229.
[11] H. Yang, F. Yan, Y. Lin, T. Wang, *ACS Sustainable Chem. Eng.* **2017**, *5*, 10215.
[12] X. Chen, X. Li, J. Sun, C. Sun, J. Shi, F. Pang, H. Zhou, *Ceram. Int.* **2020**, *46*, 2764.
[13] Y. Zhang, Z. Jiang, J. Huang, L. Y. Lim, W. Li, J. Deng, D. Gong, Y. Tang, Y. Lai, Z. Chen, *RSC Adv.* **2015**, *5*, 79479.
[14] K. Kordás, M. Mohl, Z. Kónya, Á. Kukovecz, *Transl. Mater. Res.* **2015**, *2*, 015003.
[15] M. D. Wadge, B. Turgut, J. W. Murray, B. W. Stuart, R. M. Felfel, I. Ahmed, D. M. Grant, *J. Colloid Interface Sci.* **2020**, *566*, 271.
[16] M. D. Wadge, M. J. Carrington, H. Constantin, K. Orange, J. Greaves, M. T. Islam, K. M. Zakir Hossain, T. P. Cooper, Z. R. Kudrynskyi, R. M. Felfel, I. Ahmed, D. M. Grant, *Mater. Charact.* **2022**, *185*, 111760.
[17] B. Abida, L. Chirchi, S. Baranton, T. W. Napporn, C. Morais, J.-M. Léger, A. Ghorbel, *J. Power Sources* **2013**, *241*, 429.
[18] X.-L. Sui, Z.-B. Wang, C.-Z. Li, J.-J. Zhang, L. Zhao, D.-M. Gu, S. Gu, *J. Mater. Chem. A* **2015**, *3*, 840.
[19] A. Nikhil, G. Anjusree, S. V. Nair, A. S. Nair, *RSC Adv.* **2015**, *5*, 88464.

[20] N. T. Nolan, M. K. Seery, S. C. Pillai, *J. Phys. Chem. C* **2009**, *113*, 16151.
[21] G. H. Major, N. Fairley, P. M. A. Sherwood, M. R. Linford, J. Terry, V. Fernandez, K. Artyushkova, *J. Vac. Sci. Technol., A* **2020**, *38*, 061203.
[22] B. D. Cullity, *Elements of X-Ray Diffraction*, Addison-Wesley Publishing, Massachusetts, USA **1956**.
[23] M. A. Bird, S. E. Goodwin, D. A. Walsh, *ACS Appl. Mater. Interfaces* **2020**, *12*, 20500.
[24] H. M. Kim, F. Miyaji, T. Kokubo, T. Nakamura, *J. Biomed. Mater. Res.* **1996**, *32*, 409.
[25] T. Kokubo, F. Miyaji, H.-M. Kim, T. Nakamura, *J. Am. Ceram. Soc.* **1996**, *79*, 1127.
[26] H. Eslami, F. Moztarzadeh, T. S. J. Kashi, K. Khoshroo, M. Tahriri, *Synth. React. Inorg., Met.-Org., Nano-Met. Chem.* **2016**, *46*, 1149.
[27] G.-S. Kim, H.-K. Seo, V. P. Godble, Y.-S. Kim, O. B. Yang, H.-S. Shin, *Electrochem. Commun.* **2006**, *8*, 961.
[28] L. Torrente-Murciano, A. A. Lapkin, D. Chadwick, *J. Mater. Chem.* **2010**, *20*, 6484.
[29] A. L. Papa, L. Dumont, D. Vandroux, N. Millot, *Nanotoxicology* **2013**, *7*, 1131.
[30] A. L. Papa, J. Boudon, V. Bellat, A. Loiseau, H. Bisht, F. Sallem, R. Chassagnon, V. Berard, N. Millot, *Dalton Trans.* **2015**, *44*, 739.
[31] H. Zhao, W. Dong, Y. Zheng, A. Liu, J. Yao, C. Li, W. Tang, B. Chen, G. Wang, Z. Shi, *Biomaterials* **2011**, *32*, 5837.
[32] A. Carrado, F. Perrin-Schmitt, Q. V. Le, M. Giraudel, C. Fischer, G. Koenig, L. Jacomine, L. Behr, A. Chalom, L. Fiette, A. Morlet, G. Pourroy, *Dent. Mater.* **2017**, *33*, 321.
[33] J. Gil, J. M. Manero, E. Ruperez, E. Velasco-Ortega, A. Jimenez-Guerra, I. Ortiz-Garcia, L. Monsalve-Guil, *Materials* **2021**, *14*, 2879.
[34] T. Kawai, T. Kizuki, H. Takadama, T. Matsushita, H. Unuma, T. Nakamura, T. Kokubo, *J. Ceram. Soc. Jpn.* **2010**, *118*, 19.
[35] J. Forsgren, H. Engqvist, *J. Mater. Sci. Mater. Med.* **2010**, *21*, 1605.
[36] S. Guo, D. Yu, X. Xiao, W. Liu, Z. Wu, L. Shi, Q. Zhao, D. Yang, Y. Lu, X. Wei, *J. Mater. Chem. B* **2020**, *8*, 6048.
[37] J. I. Langford, A. Wilson, *J. Appl. Crystallogr.* **1978**, *11*, 102.
[38] S. Rastegari, E. Salahinejad, *Met. Mater. Int.* **2019**, *26*, 188.
[39] K. Lee, D. Yoo, *Arch. Metall. Mater.* **2015**, *60*, 1371.
[40] S. Yamaguchi, H. Takadama, T. Matsushita, T. Nakamura, T. Kokubo, *J. Ceram. Soc. Jpn.* **2009**, *117*, 1126.
[41] T. Deepak, G. Anjusree, K. N. Pai, D. Subash, S. V. Nair, A. S. Nair, *RSC Adv.* **2014**, *4*, 27084.
[42] Z. Chang, J. Liu, J. Liu, X. Sun, *J. Mater. Chem.* **2011**, *21*, 277.
[43] Q. Zhang, T. Zhang, Y. Wei, T. Zhai, H. Li, *J. Mater. Chem. A* **2017**, *5*, 18691.
[44] M. Rutar, N. Rozman, M. Pregelj, C. Bittencourt, R. Cerc Korosec, A. Sever Skapin, A. Mrzel, S. D. Skapin, P. Umek, *Beilstein J. Nanotechnol.* **2015**, *6*, 831.
[45] R. Marchand, L. Brohan, M. Tournoux, *Mater. Res. Bull.* **1980**, *15*, 1129.
[46] H. Hantsche, *Scanning* **1989**, *11*, 257.
[47] M. Sankararaman, D. Perry, *J. Mater. Sci.* **1992**, *27*, 2731.
[48] B. Ohler, S. Prada, G. Pacchioni, W. Langel, *J. Phys. Chem. C* **2012**, *117*, 358.
[49] H. Takadama, H. M. Kim, T. Kokubo, T. Nakamura, *J. Biomed. Mater. Res.* **2001**, *55*, 185.
[50] R. Zárate, S. Fuentes, J. P. Wiff, V. Fuenzalida, A. Cabrera, *J. Phys. Chem. Solids* **2007**, *68*, 628.
[51] M. C. Biesinger, L. W. Lau, A. R. Gerson, R. S. C. Smart, *Appl. Surf. Sci.* **2010**, *257*, 887.
[52] M. C. Biesinger, B. P. Payne, B. R. Hart, A. P. Grosvenor, N. S. McIntryre, L. W. Lau, R. S. Smart, *J. Phys.: Conf. Ser.* **2008**, *100*, 012025.
[53] U. Diebold, T. Madey, *Surf. Sci. Spectra* **1996**, *4*, 227.
[54] H. M. Kim, H. Takadama, F. Miyaji, T. Kokubo, S. Nishiguchi, T. Nakamura, *J. Mater. Sci. Mater. Med.* **2000**, *11*, 555.
[55] V. Jokanović, M. Vilotijević, B. Jokanović, M. Jenko, I. Anžel, D. Stamenković, V. Lazic, R. Rudolf, *Corros. Sci.* **2014**, *82*, 180.
[56] T. Kokubo, S. Yamaguchi, *Materials* **2009**, *3*, 48.
[57] T. Mazza, E. Barborini, P. Piseri, P. Milani, D. Cattaneo, A. L. Bassi, C. E. Bottani, C. Ducati, *Phys. Rev. B* **2007**, *75*, 045416.
[58] B. C. Viana, O. P. Ferreira, A. G. S. Filho, A. A. Hidalgo, J. M. Filho, O. L. Alves, *Vib. Spectrosc.* **2011**, *55*, 183.
[59] T. Kasuga, M. Hiramatsu, A. Hoson, T. Sekino, K. Niihara, *Adv. Mater.* **1999**, *11*, 1307.
[60] H. Liu, D. Yang, Z. Zheng, X. Ke, E. Waclawik, H. Zhu, R. L. Frost, *J. Raman Spectrosc.* **2010**, *41*, 1331.
[61] Y. Su, M. L. Balmer, B. C. Bunker, *J. Phys. Chem. B* **2000**, *104*, 8160.
[62] C. Byrne, R. Fagan, S. Hinder, D. E. McCormack, S. C. Pillai, *RSC Adv.* **2016**, *6*, 95232.
[63] T. A. Centeno, F. Stoeckli, *J. Power Sources* **2006**, *154*, 314.
[64] C. C. McCrory, S. Jung, J. C. Peters, T. F. Jaramillo, *J. Am. Chem. Soc.* **2013**, *135*, 16977.
[65] X. Min, Y. Chen, M. W. Kanan, *Phys. Chem. Chem. Phys.* **2014**, *16*, 13601.
[66] R. Ma, G. Lin, Y. Zhou, Q. Liu, T. Zhang, G. Shan, M. Yang, J. Wang, *NPJ. Comput. Mater.* **2019**, *5*, 78.
[67] X. Ge, A. Sumboja, D. Wuu, T. An, B. Li, F. T. Goh, T. A. Hor, Y. Zong, Z. Liu, *ACS Catal.* **2015**, *5*, 4643.
[68] T. Shinagawa, A. T. Garcia-Esparza, K. Takanabe, *Sci. Rep.* **2015**, *5*, 13801.